Since January 2020 Elsevier has created a COVID-19 resource centre with free information in English and Mandarin on the novel coronavirus COVID-19. The COVID-19 resource centre is hosted on Elsevier Connect, the company's public news and information website.

BBA - Biomembranes 1860 (2018) 407–415

Contents lists available at ScienceDirect

BBA - Biomembranes

journal homepage: www.elsevier.com/locate/bbamem

NMR structure and localization of a large fragment of the SARS-CoV fusion protein: Implications in viral cell fusion

Mukesh Mahajan, Deepak Chatterjee, Kannaian Bhuvaneswari, Shubhadra Pillay, Surajit Bhattacharjya*

School of Biological Sciences, Nanyang Technological University, 60 Nanyang Drive, Singapore 637551, Singapore

ARTICLE INFO

Keywords:
SARS-CoV
Cell fusion
NMR
Structure
Fusion protein
Fusion peptide

ABSTRACT

The lethal Coronaviruses (CoVs), Severe Acute Respiratory Syndrome-associated Coronavirus (SARS-CoV) and most recently Middle East Respiratory Syndrome Coronavirus, (MERS-CoV) are serious human health hazard. A successful viral infection requires fusion between virus and host cells carried out by the surface spike glycoprotein or S protein of CoV. Current models propose that the S2 subunit of S protein assembled into a hexameric helical bundle exposing hydrophobic fusogenic peptides or fusion peptides (FPs) for membrane insertion. The N-terminus of S2 subunit of SARS-CoV reported to be active in cell fusion whereby FPs have been identified. Atomic-resolution structure of FPs derived either in model membranes or in membrane mimic environment would glean insights toward viral cell fusion mechanism. Here, we have solved 3D structure, dynamics and micelle localization of a 64-residue long fusion peptide or LFP in DPC detergent micelles by NMR methods. Micelle bound structure of LFP is elucidated by the presence of discretely folded helical and intervening loops. The C-terminus region, residues F42-Y62, displays a long hydrophobic helix, whereas the N-terminus is defined by a short amphipathic helix, residues R4-Q12. The intervening residues of LFP assume stretches of loops and helical turns. The N-terminal helix is sustained by close aromatic and aliphatic sidechain packing interactions at the non-polar face. $^{15}N\{^{1}H\}$NOE studies indicated dynamical motion, at ps-ns timescale, of the helices of LFP in DPC micelles. PRE NMR showed that insertion of several regions of LFP into DPC micelle core. Together, the current study provides insights toward fusion mechanism of SARS-CoV.

1. Introduction

The enveloped viruses transfer genetic materials into the host cell through a well-orchestrated cell fusion process. Viral fusion proteins, anchored in the membrane, play dominant role in the fusion process. The fusion protein machinery connects membranes of the virus and host cells leading to the cell fusion. Fusion proteins consists of two subunits namely receptor binding and membrane fusion [1–4]. Conformational transition of fusion protein often exposes buried hydrophobic fusion peptide from the core structure. Fusion peptide inserts into the outer leaflet of the plasma membrane of the host cell initiating membrane fusion process [5–9]. Understating fusion mechanism not only garners knowledge of virus pathology but also can be exploited for the development of antiviral drugs [10–14]. Consequently, atomic-resolution structures of fusion proteins have provided important molecular insights for the membrane fusion process [2,4,15–19]. However, it may be a daunting task to obtain membrane embedded structures of full-length fusion proteins. To fill the gap, atomic resolution structures and functional analyses, in lipid bilayer or in membrane mimic environments, of FPs are frequently considered [20–28].

In humans, CoVs are known to cause mild cold and other nonlethal diseases, however, SARS-CoV and recently emerged MERS-CoV are global health risk [29–32]. Pandemic SARS-CoV outbreak in 2002–2003 caused ~800 deaths and 9000 cases of infections over 29 countries. In 2012, MERS-CoV has been identified in Middle East and England which was rapidly spread over 29 countries [29,33–35]. According to WHO, MERS-CoV has caused over 1800 infections and 422 related deaths. Despite potential threat for the large scale outbreaks of SARS and MERS, no drugs or vaccines of therapeutics modality are available so far. Therefore, understating of the molecular mechanism of viral pathogenesis may be exploited for the development of anti-viral drugs and vaccines [36,37].

It is well established that the host cell receptor binding and membrane fusion occur through the S1 and S2 subunits of spike (S)

Abbreviations: CoVs, Coronaviruses; SARS-CoV, Severe acute respiratory syndrome-associated coronavirus; FPs, fusion peptides; LFP, long fusion peptide; NMR, nuclear magnetic resonance; DPC, dodecyl phosphocholine; PRE, paramagnetic relaxation enhancement

* Corresponding author at: 60 Nanyang Drive, 637551, Singapore.
E-mail address: surajit@ntu.edu.sg (S. Bhattacharjya).

https://doi.org/10.1016/j.bbamem.2017.10.002
Received 4 May 2017; Received in revised form 16 September 2017; Accepted 3 October 2017
Available online 05 October 2017
0005-2736/

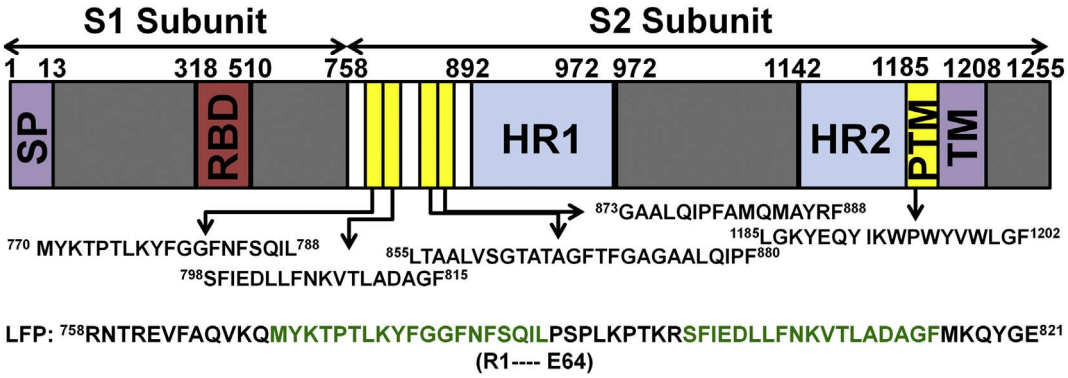

Fig. 1. Functional domains of the spike glycoprotein or S protein of SARS-CoV. S protein contains two subunits, S1 subunit is involved in receptor binding by RBD domain (in red), the S2 subunit mediates cell membrane fusion utilizing coiled-coiled HR1 and HR2 domains (in light blue), FPs (in yellow) located upstream of HR1 and PTM (in yellow) close to the TM domain. The amino acid sequences of FPs are shown. The primary structure of 64-residue LFP construct, studied here, encompasses residues R758-E821, labelled as R1-E64.

glycoprotein of SARS-CoV [38–40]. SARS-CoV fusion protein or the S2 subunit belongs to the class I type fusion system that contains two heptad repeats, HR1 and HR2, and a TM domain at the C-terminus [41–47]. HR1 and HR2 complex stabilizes six helix bundle topology or trimer-of-hairpins structure, a canonical feature shared by the class I fusion proteins [41–47]. Interestingly, multiple regions of S2 subunit have been identified with fusogenic activity (Fig. 1). As seen, potential FPs are largely mapped upstream of HR1 in the S2 subunit of fusion protein (Fig. 1). These potential FPs demonstrated vesicle fusion, membrane partitioning and membrane disordering [48–55]. It has been proposed that the cell-cell fusion may involve a concerted action of the HR1 and HR2 along with insertion of the FPs into cell membrane [48,50,54]. Atomic-resolution structure of SARS-CoV FPs in membrane or in membrane mimic environment can provide mechanistic insights toward virus-cell fusion. Previously, utilizing synthetic peptides, we reported NMR structures of three potential FPs of SARS-CoV, namely residues M770-L788, residues G873-F888 and residues L1185-F1202, in DPC micelle [56]. Conceivably, during cell-cell fusion multiple FPs may insert into membrane therefore, here, we investigated a long fusion peptide (LFP) encompassing residues R758-E821 (Fig. 1). The 64-residue LFP was over-expressed in *E. coli* cells as a fusion protein containing prodomain of human furin at the N-terminus and further purified. NMR structural characterization was carried out using isotopically labelled LFP in DPC detergent solution. 3D structure of LFP and localization in micelle may aid toward better understating of cell-cell fusion and perhaps assist in antiviral drug development.

2. Materials and methods

2.1. Chemicals

1,2-Dimyristoyl-sn-Glycero-3-Phosphocholine (DMPC), Rho−PE (N-(lissamine rhodamine B-sulfonyl) dioleolylphosphatidylethanolamine) and NBD−PE (N-(7-nitrobenz-2-oxa-1,3-diazol-4-yl)dioleoylphosphatidylethnaolamine) were purchased from Avanti polar lipids (Alabaster, AL). Spin-labelled lipids 5-doxyl-stearic acid (5-DSA), 16-doxyl-stearic acid (16-DSA) and triton-X-100 were purchased from Sigma (St. Louis, MO). Perdeuterated dodecylphosphocholine (DPC-d_{38}), ^{15}N ammonium chloride, ^{13}C glucose were obtained from Cambridge Isotope Inc. All other chemicals were of analytical grades.

2.2. Over-expression and purification of LFP in E. coli

LFP was over-expressed in *E. coli* cells as a fusion protein containing 81 amino acid long human prodomain at the N-terminus [57–59]. A synthetic gene, with *E. coli* optimized codons, of the fusion protein was cloned (Shanghai ShineGene Molecular Biotech™) in a pET14b vector containing a six His-tag at the N-terminus for affinity purification of the fusion protein and a D-P sequence was introduced between the prodomain and LFP for formic acid mediated digestion of the fusion protein [57–59]. Note, in the synthetic gene of LFP, codon of residue Asp890 was changed to a codon of amino acid Ser to remove an internal D-P site in the LFP. Plasmid DNA was transformed into *E. coli* BL21 (DE3) (Novagen) cells using heat shock method. Transformed cells were prepared on a LB agar plate with ampicillin and allowed to grow overnight at 37 °C. Fusion protein was over-expressed in *E. coli* BL21 (DE3) cells, either on LB or M9 minimal medium containing ^{15}N labelled ammonium chloride and/or ^{13}C labelled glucose by IPTG induction, $OD_{600} \sim 0.6–0.8$, for 12 h at 37 °C. Cell mass was harvested by centrifugation at 7000 rpm and re-suspended in a denaturing buffer A (50 mM sodium phosphate buffer, 100 mM NaCl, 8 M urea and 5 mM imidazole, pH 7.5) followed by lysis using sonication for 15 min. This translucent cell suspension was further centrifuged at 18000 rpm and the supernatant was loaded onto pre-equilibrated Ni-NTA agarose beads column. The column was further treated with a wash buffer, 50 mM sodium phosphate, 100 mM NaCl, 8 M urea and 20 mM imidazole, pH 7.5 to remove non-specific bound proteins. The fusion protein was eluted from Ni-NTA column using buffer A containing 500 mM imidazole. The molecular weight and purity of the fusion protein was judged by SDS-PAGE. Purified fusion protein was dialyzed against water for 15–20 h to remove urea leading to precipitation of the expressed protein. Precipitated fusion protein was solubilized in 70% formic acid at 40 °C to release LFP by D-P peptide bond cleave [60]. Digestion of fusion protein was monitored using SDS-PAGE gel by taking samples at various time intervals. Almost complete digestion of the fusion protein can be seen after 20 h of incubation in formic acid solution. Post digestion, formic acid was removed using a rotary evaporator under vacuum yielding a thin film. The thin film was solubilized in buffer A and pH was adjusted to 7.5 and loaded into Ni-NTA column. As, uncleaved fusion protein and cleaved furin prodomain remained bound to the column, LFP was eluted in the flow through. LFP samples were further purified to homogeneity by use of RP-HPLC in C4 column (300 Å pore size, 5 μM particle size) using a linear gradient of 10% acetonitrile/90% water mixture. The LFP was eluted as a major peak fraction at 30 min. The mass of LFP, 7556 Da, was confirmed by MALDI-TOF mass spectrometry.

2.3. NMR spectroscopy and data processing

NMR samples were prepared by dissolving dry lyophilized powder of LFP (0.5 mM) in aqueous solution containing 125 mM DPC-d_{38} and 10% D_2O, pH 4.7. Chemical shift of ^1H was referenced to DSS (Sodium 2, 2-Dimethyl- 2-Silapentane-5-Sulfonate). ^{15}N and ^{13}C chemical shifts were indirectly reference using frequency ratios of $^{13}C/^1H$ and $^{15}N/^1H$ [61]. NMR data were acquired using a Bruker AVANCE II 600 MHz spectrometer equipped with a cryoprobe. Sample temperature was fixed

at 30 °C. Standard triple resonance experiments HNCA, HN(CO)CA, HNCACB and CBCA(CO)NH were acquired to make sequence-specific backbone and sidechain C^{β} resonances. Further, 3-D ^{15}N TOCSY-HSQC and ^{15}N NOESY-HSQC experiments were performed for assignment of protons and NOEs. ^{15}N–edited [^{1}H,^{1}H]-NOESY, HNCOCA, HNCA, CBCACONH and HNCACB experiments were obtained with complex data points of 64(F1)·40(F2)·2048(F3) whereas ^{15}N–edited [^{1}H,^{1}H]-TOCSY spectra were acquired with 56(F1)·40(F2)·2048(F3) complex point. Mixing time for ^{15}N–edited [^{1}H,^{1}H]-TOCSY and NOESY were kept at 80 ms and 200 ms, respectively. NMR data were processed and analyzed using TopSpin 3.0 (Bruker) and SPARKY 3.113 (T. D. Goddard and D. G. Kneller, University of California, San Francisco, CA), respectively. For paramagnetic relaxation enhancement (PRE) studies, ^{15}N–^{1}H HSQC spectra of LFP were acquired in the presence of spin labelled lipids, 5-doxylstearic acid (5-DSA) and 16-doxylstearic acid (16-DSA) at 1 mM. ^{15}N-{^{1}H} heteronuclear NOE experiments were performed with and without saturating ^{1}H resonances. ^{1}H resonances were saturated for 2.5 s by 120° pulses spaced at 5 ms interval with a cycle delay of 2 s. A total of 2048 × 128 complex increments were collected for ^{15}N-{^{1}H} heteronuclear NOE experiments. Heteronuclear NOEs were determined as the ratio of the peak intensities with and without saturation.

2.4. Structure calculations

The DPC-bound structure of SARS-CoV fusion peptide was calculated using CYANA 2.1. Briefly, structure calculations were performed with 200 conformers with random torsion angle values. A total of 10,000 torsion angle dynamics steps were performed for each of the conformer during standard simulated annealing. Restrained energy minimization was carried out on twenty conformers with lowest final target function values. Seven cycled were used to generate final 20 conformers. Ramachandran plot revealed no disallowed region.

2.5. Liposome fusion assays

LFP mediated liposome fusion was studied by fluorescence resonance energy transfer (FRET) between NBD—PE (donor) and Rho—PE (acceptor) [62,63]. LUVs were made using DMPC lipid. Labelled LUVs were prepared by mixing 5 mM unlabelled LUV with 0.05 mM of NBD—PE and 0.05 mM of Rho—PE. Unlabelled and labelled LUV samples were passed through 100 nm filter using an extruder to produce uniform sized SUVs. 100 μM of unlabelled and 25 μM of labelled liposomes were mixed together and basal fluorescence spectra of NBD (an excitation wavelength of 470 nm, λ_{max} emission 530 nm) were recorded. Experiments were carried out in 10 mM sodium phosphate buffer, pH 4.8. Various concentrations of LFP, 20, 40, 60, 80, 100 μM, were added to the liposome, from a stock solution and fluorescence was measured. The percentage of lipid mixing was estimated using the equation $[(F\text{-}F_0)/(F_{max}\text{-}F_0)]$*100 where F_0 and F represent fluorescence intensity of the NBD probe either in the absence or presence of LFP, respectively, F_{max} is the maximum fluorescence intensity observed for NBD after the addition of 10% Triton-X-100.

3. Results

3.1. Fusion peptides (FPs) of SARS-CoV

Several research groups have identified and characterized peptide fragments derived from the S2 subunit of S protein of SARS-CoV [48–52,55]. Based on the previous reports, the S2 subunit of S protein contains four potential FPs located at the N-terminus of HR1 domain [48–52] and an aromatic rich pre-transmembrane region or PTM adjacent to the C-terminal TM [55] (Fig. 1). Among these four FPs, fusogenic activity corresponding to the residues Y855-F880 has recently been reported [52] (Fig. 1). This FP, residues Y855-F880, appeared to contain overlapping region with residues G873-F888 (Fig. 1). We solved 3D structures, in DPC detergent micelle, of three synthetic fusogenic peptides, termed FP (fusion peptide): residues M770-L788, IFP (internal fusion peptide): residues G873-F888 and PTM: residues L1185-F1202 [56]. The presence of an adjacent FP in the S protein of SARS-CoV has prompted us determine 3D structure of a longer fragment, 64-amino acid, or the LFP construct (Fig. 1). The LFP construct contains two FPs that is connected by a linker rich in Pro and basic amino acids. The N-terminus of LFP further extends to include residues at the proteolytic cleavage site (Fig. 1). The 64-residue LFP has been over-expressed and isotopically labelled for NMR studies (Materials and Methods).

3.2. Liposome fusion by LFP of SARS-CoV

Membrane fusion activity of FPs can be estimated using a FRET-based assay of lipid mixing [62,63]. In this assay, liposomes were made containing fluorescently labelled lipids typically NBD—PE (donor) and Rh-PE (acceptor) and mixed with unlabelled liposome. In the event of membrane fusion between unlabelled and labelled liposomes, mediated by a peptide, FRET efficiency decreases due to a dilution of the FRET pair that is reflected by an increase of NBD—PE fluorescence for labelled liposome [62]. We examined lipid mixing mediated by LFP using labelled and unlabelled DMPC liposomes and percentage of lipid mixing was estimated (see Materials and Methods). The liposome fusion assays mediated by LFP were performed at pH of 4.8. Note, SARS fusion peptide demonstrated higher lipid mixing at a lower pH that may potentially indicated stabilization of fusion active conformations under such conditions [55]. Further, it has been demonstrated that host-SARS virus cell fusion can occur at the acidic environment of endosomes [64]. Fig. 2 shows the percentage of lipid mixing mediated at various molar ratios of LFP/lipid. As expected, LFP demonstrated lipid mixing activity in a dose dependent manner, suggesting its fusogenic potential (Fig. 2). At a peptide/lipid ratio of 1, approximately 32% lipid mixing was estimated (Fig. 2). A direct comparison of fusogenic activity between the LFP and the short fusion peptides appeared to be less straight forward due to different lipid compositions, and parameters used e.g. leakage, partitioned coefficient, to determine fusogenic activity [49,54,55]. Nonetheless, membrane fusion studies demonstrated low fusogenic activity, ~10%, of M770-L778 peptide in PC liposomes [54]. Whereas, the fusion peptide S789-F815 showed higher membrane fusion, estimated to be 40% in PC/PS/cholesterol liposomes [55]. It may be noted that peptide S789-F815 contained additional Lys residues at the C-

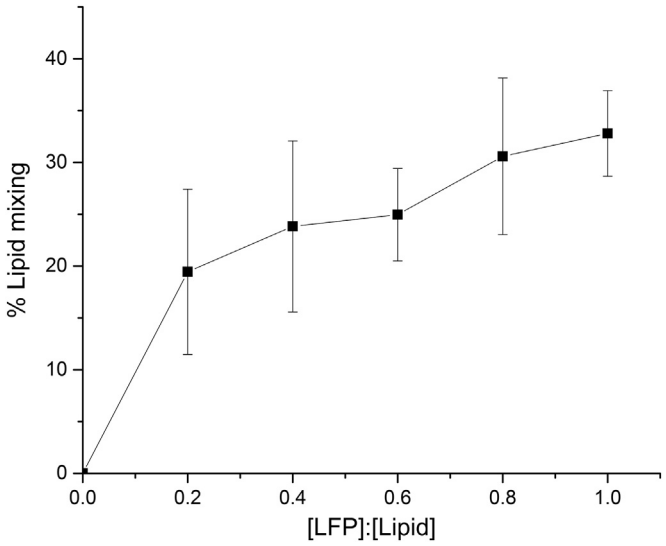

Fig. 2. DMPC liposome fusion mediated by LFP. Plot shows % lipid mixing as a function of LFP/lipid molar ratios obtained from FERT analyses.

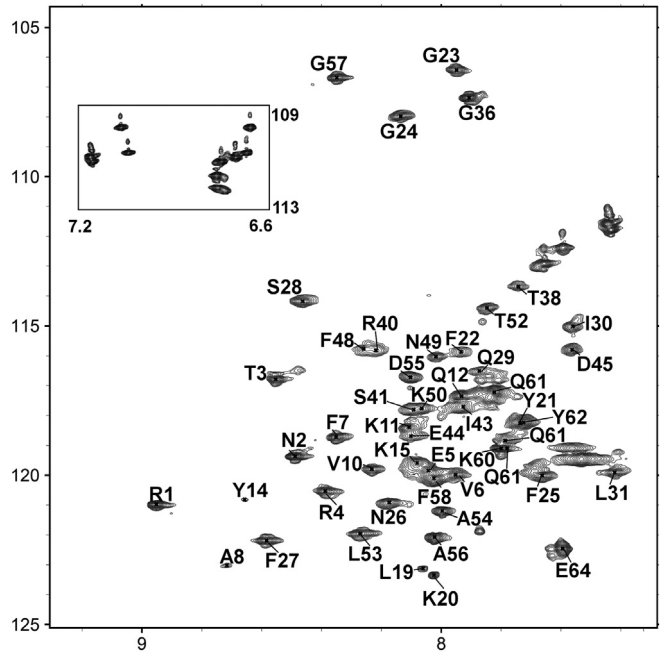

Fig. 3. $^{15}N-^{1}H$ HSQC spectrum of LFP in 125 mM perdeuterated DPC micelles solution. The HSQC peaks showing assignment to individual residue were assigned utilizing 3-D triple resonance NMR experiments.

terminus that may modulate the extent of membrane fusion [55]. In order to obtain a clear comparison of the fusogenic activity across the different peptides, membrane fusion studies may be carried out under similar lipid environments.

3.3. Resonance assignments and conformation of LFP in DPC detergent solution

$^{15}N-^{1}H$ HSQC spectra of LFP were acquired in SDS and DPC detergent solutions. $^{15}N-^{1}H$ HSQC spectra obtained in DPC micelle solution showed better dispersion and more number of resolved peaks, therefore, all 3-D NMR experiments were conducted in solution of DPC micelle. Fig. 3 shows $^{15}N-^{1}H$ HSQC spectrum of LFP in DPC micelle indicating assignments. $^{15}N-^{1}H$ HSQC peaks were assigned based on the standard triple resonance experiments HNCA, HN(CO)CA, CBCA(CO)NH and HNCACB. Out of 60 non-prolyl residues, $^{15}N-^{1}H$ HSQC peaks could be identified for 49 amino acids (Fig. 3). HSQC crosspeaks of a stretch of residues S33, L35, K36 and K39 and residue T16 cannot be assigned due to the presence of multiple Pro in the sequence (Fig. 1). HSQC crosspeaks of few more residues F42, L46, L47 and V51 were ambiguous due to overlapping resonances. Secondary chemical shift or chemical shift deviation from random coil of $^{13}C\alpha$ of LFP was utilized to obtain secondary structures in DPC micelle (Fig. 4). Amino acid residues in α-helical conformations would exhibit positive secondary chemical shift of $^{13}C\alpha$ [65]. By contrast, an opposite trend has been observed for residues in β-type or β-sheet conformations [64]. In particular, based on the secondary chemical shift of $^{13}C\alpha$, populated helical or β-sheet conformations can be delineated over a stretch of five or three residues, respectively. As seen, LFP delineated positive secondary chemical shift for many contiguous residues (Fig. 4). Notably, residues encompassing T3-K11 at the N-terminus of LFP demonstrated diagnostic secondary chemical shift of helical conformations (Fig. 4). Several residues, at the C-terminus of LFP, e.g. residues I44-Y62, with interruptions at residues D55 and F58, also delineated positive secondary chemical shift, indicating populated α-helical conformations (Fig. 4). By contrast, intervening residues of LFP showed either negative or positive secondary chemical shifts within short span of residues (Fig. 4).

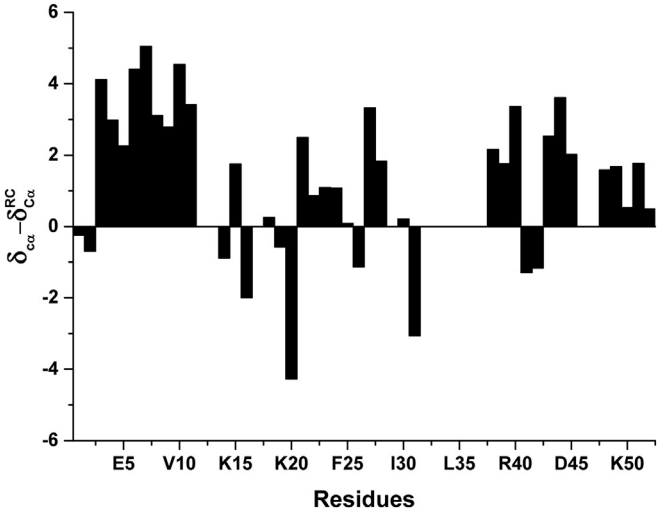

Fig. 4. Bar diagram showing secondary chemical shift or chemical shift deviation of $^{13}C\alpha$ ($\delta_{C\alpha}$) from random coil value ($\delta^{RC}_{C\alpha}$) of residues of LFP in DPC micelle solution. Secondary chemical shift cannot be obtained for Pro residues and for some residues either located in Pro rich region or with overlapping resonances.

Table 1
Structural statistics of twenty lowest energy structures of LFP in DPC micelles.

Distance constraints	
Short range (i-j) ≤ 1	99
Medium range [1 < |i-j| ≤ 4]	83
Long-range [|i-j| ≥ 5]	3
Total	185
Angle constraints	
ϕ, ψ constraints	60
Deviation from mean structure (Å) (backbone atoms)	
Residues 4–12	1.52
Residues 13–42	8.83
Residues 43–59	2.44
Ramachandran plot for the mean structure[a]	
% residues in the most favored region	90.9
% residues in the additionally allowed region	7.3
% residues in the generously allowed region	1.8
% residues in the disallowed region	0.0

[a] Calculated using Procheck.

3.4. 3-D structure of LFP in DPC detergent solution

An ensemble of conformations of LFP was determined, based on NOE driven distance and dihedral angle (Φ, Ψ) constraints using CYANA [66]. The structural statistics are provided in Table 1. Fig. 5 (left panel) shows superposition of twenty low energy structures, for three individual segments namely residues R4-Q12 (panel A), residues I43-M59 (panel B) and residues M13-F42 (panel C) of LFP, for the backbone atoms (Cα, N and C′). The N- and C-termini, residues R4-Q12 and residues I44-M59, are found to be closely superposed with backbone RMSD value of 1.52 Å and 2.2 Å, respectively (Table 1). By contrast, the middle segment of LFP shows large variation among superposed conformations (Fig. 5, panel C). In other words, residues at the N- and C-termini regions are uniquely folded whereas residues located at the middle of LFP experienced more conformational variable. Fig. 5D shows a representative structure of LFP in DPC micelle. Essentially, 3-D structure of LFP in DPC micelle is defined by a short N-terminus helix, residues R4 to Q12 and a relatively longer helix at the C-terminus that appears to be extended from residues I43-Y62, with a kink at residue D55 (Fig. 5D). Further, residues M13-F25 and residues F27-I30 delineated a long loop and a single turn of helix, respectively (Fig. 5, panel D). The Pro rich segment, residues $P^{32}SPLKP^{37}$, of LFP assumed rather

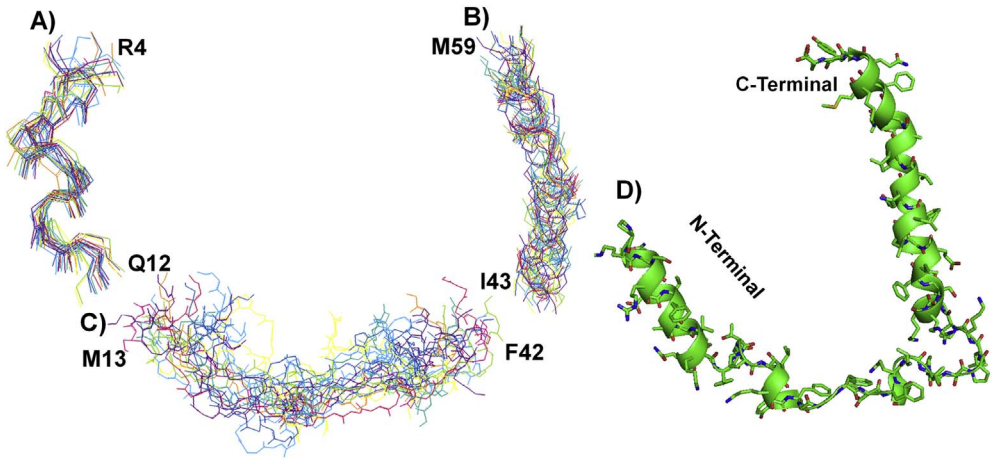

Fig. 5. Superposition of twenty low energy structures of LFP determined using CYANA, showing residues R4-Q12 (panel A), residues I43-M59 (panel B) and residues M13-F42 (panel C). (panel D) Ribbon depiction of a representative structure of LFP in DPC micelles.

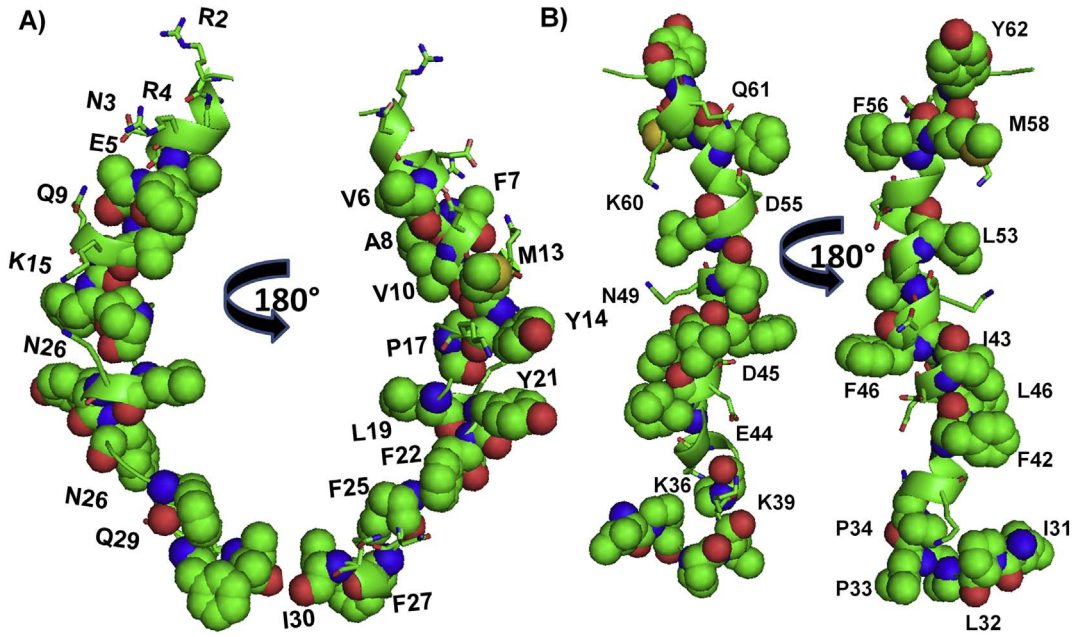

Fig. 6. Sidechain disposition and packing of residues of LFP at the N-terminus (panel A) and C-terminus (panel B) in two different orientations. The hydrophobic and aromatic residues are presented in space-fill whereas polar and charged residues are shown as thick sticks. The N- and C-termini helices are marked as ribbon (in green). C, N, O and S atoms are shown in green, blue, red and yellow colors, respectively.

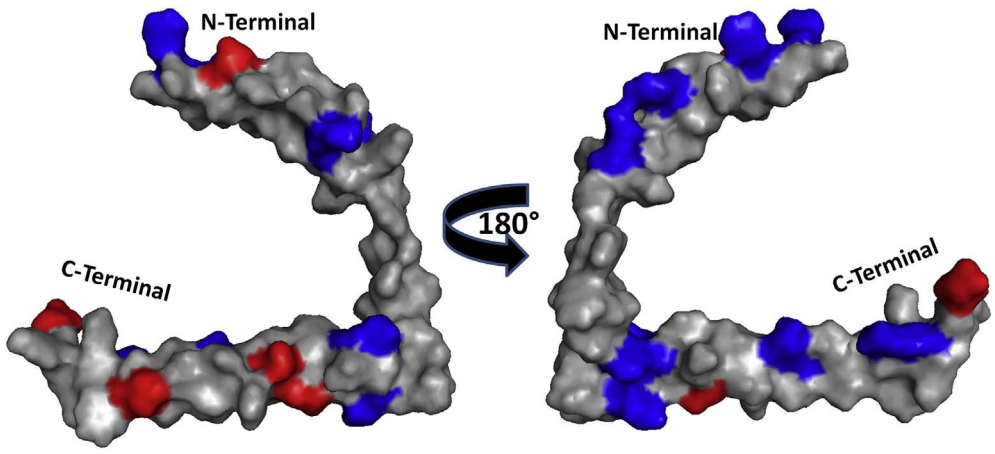

Fig. 7. Electrostatic surface diagram of a representative structure of LFP in DPC micelles. Hydrophobic residues, positively charged residues and negatively charged residues are shown in grey, blue and red colors, respectively.

extended conformation, whereas a short helical conformation could be deduced for residues $T^{38}KR^{40}$ (Fig. 5, panel D). The N-terminal helix of LFP demonstrated an amphipathic disposition of the sidechain orientation (Fig. 6, panel A). In particular, the hydrophilic face of the N-terminal helix is constituted by residues R4, E5, Q9 and Q12. The cationic sidechain of K11 also points toward the polar face of the helix.

Notably, the cationic sidechain of residue K15, belonging to the adjacent loop, further extends the polar face of the helix (Fig. 6, panel A). There are potential ionic and/or hydrogen bond interactions among the residues in the polar face of the helix. The anionic sidechain of residue E5 is in close proximity to the guanidinium sidechain of residue R1. Further, spatial proximity among the sidechains of residues Q9/Q12, R1/Q9, R1/Q12 and K15/Q12 perhaps can potentially form hydrogen bond interactions at the hydrophilic face of the N-terminal helix (Fig. 6, panel A). The nonpolar face of the N-terminal helix is realized by packing of hydrophobic sidechains of residues T3, V6, F7, V10 that may be further extended by loop residues M13 and Y14 (Fig. 6, panel A). In a marked contrast, the C-terminal long helix of LFP is typified by the preponderance of nonpolar and aromatic residues (Fig. 6, panel B). A large hydrophobic face of the C-terminal helix is maintained by close packing among sidechains of residues e.g. F42, I43/L46, L47/V51, F48/V51, T52 and F58,M59/Y62 (Fig. 6, panel B). The charge and polar residues of the C-terminal helix e.g. E44, D45, N49, K50, D55 and K60 are rather interdigitated among the hydrophobic sidechains that lack clear hydrophilic surface (Fig. 6, panel B). However, there are few potential polar interactions as revealed by spatial proximity of sidechains of residues D45/N49 and residues E44/K39 (Fig. 6, panel B). Fig. 7 shows a surface diagram of LFP structure displaying large nonpolar surfaces of the C-terminal helix, connecting loop residues and part of the N-terminal helix.

3.5. Backbone mobility of LFP in DPC detergent solution by heteronuclear NOE

^{15}N-{^{1}H} heteronuclear NOE experiments were utilized to probe backbone mobility, at ps-ns time scale, of the N−H bond vectors of residues of LFP in DPC micelle. Het-NOEs are plotted as a function of residue and mapped onto the structure of LFP (Fig. 8, panels A and B). As seen, several residues at the N-terminal helix, R4-Q13, exhibited high Het-NOE values, > 0.5, with an average of 0.67. Further, residues, except F48, resided in the long C-terminal helix, residues I43-Y62, of LFP demonstrated Het-NOE value ranging from 0.4 to 0.7, with an average value of 0.56 (Fig. 8, panels A and B). These observations demonstrate that the helical structures of LFP in DPC micelle are well folded and lack large motional freedom. Although, few residues, V6, A8 and Q9, of the N-terminal helix demarcated below average Het NOE values, implying local flexibility of these residues (Fig. 8, panels A and B). In addition, residues T3, T38, R40 and S41, adjacent to the helices, delineated high Het NOE, ~0.7. Note, a stretch of contiguous residues Y22, F23, G24, G25, F26, and N27 are also found to be motionally rigid, as judged by high Het NOEs (Fig. 8, panels A and B). Taken together, the Het NOE data indicated that LFP in DPC micelle contains restricted backbone motion including the N- and C-terminal helices and also for the loops and short helices at the middle.

3.6. Localization of LFP in DPC micelle by PRE probes

Micelle association and insertion of LFP was investigated by acquiring ^{15}N−^{1}H HSQC spectra either in absence or in presence of 1 mM spin labelled lipids, 5-DSA and 16-DSA. These nitric oxide spin labelled lipids can be readily inserted into detergent micelle and perturb resonances of micelle interacting molecules by enhancing relaxation [67,68]. Amino acid residues penetrated deep into the micelle may be perturbed preferentially by 16-DSA whereas surface localized residues mostly experience PRE effect from 5-DSA probe [67,68]. Fig. 9 shows residual intensity of ^{15}N−^{1}H crosspeaks estimated from HSQC spectra for individual amino acid of LFP in 5-DSA (panel A) and 16-DSA (panel B). As can be seen, most of the residues demonstrated PRE probes mediated perturbation, indicating micelle association of LFP. However, 16-DSA mediated perturbation has affected more residues compared to 5-DSA probe as evident from < 1 ratio of 16-DSA/5-DSA perturbation (Fig. 9, panel C). 16-DSA mediated perturbation appeared to be even

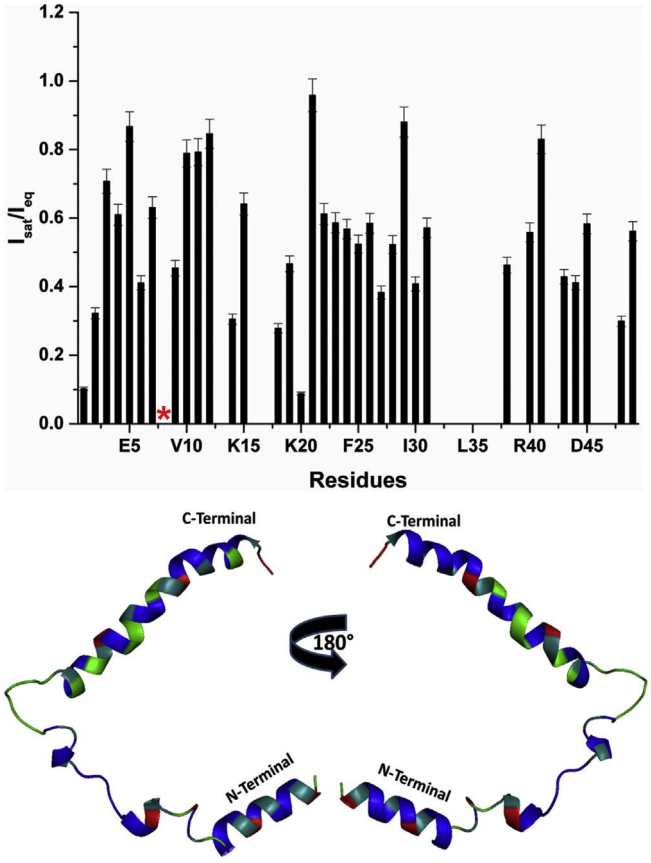

Fig. 8. (left panel) Bar diagram showing ^{15}N-{^{1}H} heteronuclear NOE values for individual residues of LFP in DPC micelle. Residue A8 showed zero Het NOE and marked as * in the plot. Heteronuclear NOE cannot be obtained for Pro residues and for some residues either located in Pro rich region or with overlapping resonances. (panel B) Ribbon representation (in green) of the backbone structure of LFP highlight ^{15}N-{^{1}H} heteronuclear NOE values as blue: > 0.5, cyan: 0.2–0.5 and red: < 0.2. Residue Pro or residues showing overlapping resonances where ^{15}N-{^{1}H} heteronuclear NOE cannot be obtained are marked in green.

higher, ratios of ≤ 0.5, for several residues located at the central region of LFP (Fig. 9, panel C). On the other hand, residues at the N- and C-termini delineated relatively lower ratios (Fig. 9, panel C). These data demonstrate that the central region of LFP may be deeply inserted into the hydrophobic core of the micelle, whereas, the N- and C-termini residues may be experiencing a relatively shallower micelle penetration (Fig. 9, panel D).

4. Discussion

All enveloped viruses utilize fusion proteins to enter into host cells mediated by membrane fusion. Based on the post fusion conformations, fusion proteins are categorized as class I, II and III [1–4]. FPs are vital in cell-cell fusion process since isolated FPs demonstrated direct interactions with membrane lipids and membrane fusion. Bioinformatics, functional mapping and membrane interactions studies indicated five disparate regions of S protein of SARS-CoV as potential FPs [48–56] (Fig. 1). Observations of as many as four FPs N-terminus of HR1 may perhaps suggest that the polypeptide segment in this region could be important for membrane fusion. Notably, multiple potential FPs have also been reported for other viral fusion proteins [69–71]. It is conceivable that multiple FPs and also adjacent regions are likely to be inserted, in a concerted manner, into the host cell membrane leading to an efficient cell-cell fusion. Previously, using synthetic peptides, we determined structures of two FPs, M770-L788 and G873-F888 and the C-terminal PTM domain L1185-F1202 in DPC detergent solution

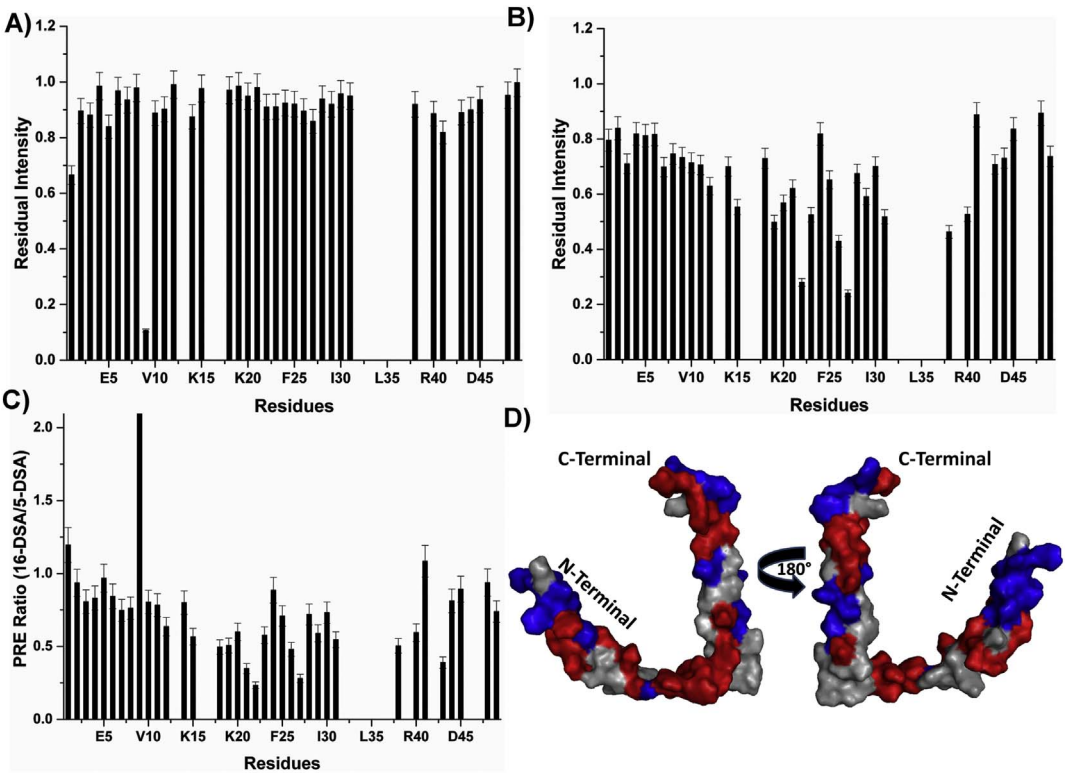

Fig. 9. Bar diagrams (panels A, B and C) showing residual intensity of HSQC peaks of LFP in PRE probes 1 mM each of 5-DSA (panel A), 16-DSA (panel B) and ratio of 16-DSA/5-DSA (panel C) in DPC detergent solution. PRE cannot be obtained for Pro residues and for some residues either located in Pro rich region or with overlapping resonances. (panel D) PRE effect mapped onto the structure of LFP, residues preferentially perturbed either by 5-DSA and 16-DSA are marked by blue or red colors, respectively. Residue Pro or residues showing overlapping resonances where PRE effect cannot be obtained are in grey color.

(Fig. 1) [56]. The current construct of 64-residue LFP contains M13-L31 or M770-L788 segment along with a structurally uncharacterized FP, residues S41-F58 or S798-F815 (Fig. 1) [55]. In order to gain insight into membrane fusion mechanism of SARS-CoV, here we have investigated liposome fusion activity and solved the 3-D structure of LFP, in DPC micelle.

The 64-residue LFP demonstrated bipartite helical and extended conformations. The N-terminus of LFP assumes an amphipathic helical structure, residues R4-Q12, followed by residues M13-L19 adopted loop like conformations (Fig. 5). Residues K20-I30 delineated two short stretches of helix connected by a loop, whereby the aromatic ring of residues F22 and F27 are in close packing interactions (Fig. 6). It is noteworthy that residues M13-L31, in isolation, largely formed a compact helical structure with bends observed at residues G23-G24 [56]. However, these residues M13-L31 in LFP assumed rather discontinuous helical and extended conformations (Fig. 5). These observations potentially indicate that the adjoining sequences of fusion proteins might influence conformations of FPs. Note, influenza hemagglutinin FPs showed large structural differences depending on the length of the amino acid sequences [24,25]. A recent study, using solid state NMR in lipid bilayer, has deduced close and semi-closed structural states of the hemagglutinin FP [72]. The determination of an amphipathic helical structure at the N-terminus of FP, in DPC micelle, may be considered as a novel feature of the SARS-CoV fusion protein. The N-terminal helical segment of LFP in DPC micelle demonstrated motional rigidity (Fig. 8) and found to be inserted into the micelle core (Fig. 9). It is likely that the N-terminal helix of the fusion protein of SARS-CoV may be important for membrane fusion activity. The C-terminal half of LFP is defined by a 20-residue long helix, residues F42-Y62, that essentially encompasses the entire distal FP, except Ser42 (or Ser798), (Figs. 1 and 5). The C-terminal helix can be further extended to include residues K39-R40 with a hinge at S42 (Fig. 5). The Pro rich sequence appeared to adopt extended conformations (Fig. 5). As seen, the C-terminus helix of LFP contains a large nonpolar surface with shallow patches of polar regions (Fig. 7). The nonpolar surface of the C-terminal helix including the residues located in the adjacent loop of LFP could be deeply inserted into the hydrophobic core of micelle (Fig. 9). Further, ^{15}N-{^{1}H} heteronuclear NOE data demonstrated that many residues belonging to the C-terminus helix is motionally rigid in DPC micelle (Fig. 8). Functional assays, by Ala scanning mutagenesis, demonstrated that the hydrophobic residues of the C-terminal helix of S2 fusion protein are critical for cell-cell fusion [55]. Recent studies have determined prefusion structures of S proteins of coronaviruses that are homologous to SARS-CoV [73,74]. Interestingly, the C-terminal LFP region has been found to be adopting helical conformations that was buried inside the prefusion protein complex [73,74]. As noted, S proteins of coronaviruses including SARS-CoV differ from influenza virus and HIV-1 [74]. In particular, the S protein of SARS-CoV contains a larger segment upstream of HR1. In the prefusion state, this polypeptide segment has been found to be buried and adopted helical conformations [74]. Peptide derived from this intervening region showed membrane interactions and fusion [48–50,52–55]. Therefore, it has postulated that membrane fusion process mediated by coronaviruses and SARS-CoV could be different from other type I viral fusion proteins [29,38,50,51,54,74]. FPs may experience conformational variations depending on lipid or detergent micelle environments [24,25,72,75]. The potential influence of the curved DPC micelles on the 3-D structure and dynamics of LFP cannot be ascertained at this point. Notably, determination of atomic resolution structure of large fusion protein like LFP embedded in lipid bilayer could be highly challenging. Regardless, atomic resolution structure of LFP of SARS-CoV, in complex of zwitterionic DPC micelle, and its localization within micelle core obtained in this study can perhaps aid in better understating of membrane fusion mechanism. The S protein mediated membrane fusion requires helical coiled-coil complex of HR1 and HR2 and multiple FPs leading to the formation of fusion pore [54,56]. The extended helical structures of LFP

along with the FPs, at the N- and C-termini, may be inserted into membrane aligning with HR1 and HR2 helices that may essentially enhance the process of membrane mixing and pore formation. In addition, FPs of SARS-CoV were found to inhibit viral infection perhaps due to their interactions with cell membranes [76,77]. Therefore, we surmise that atomic-resolution structure of LFP and membrane fusion mechanism may be further utilized for the development of drugs against SARS.

Transparency document

The Transparency document associated with this article can be found, in online version.

Acknowledgement

This work has been supported by the research grants, RG49/10 and RG11/12, from the Ministry of Education (MOE), Singapore. The pdb coordinates and associated NMR parameters are deposited to RCSB Protein Data Bank and BMRB data bank with accession numbers: PDB ID 5XJK, BMRB ID 36080.

References

[1] J.J. Skehel, D.C. Wiley, Receptor binding and membrane fusion in virus entry: the influenza hemagglutinin, Annu. Rev. Biochem. 69 (2000) 531–569.
[2] D.M. Eckert, P.S. Kim, Mechanisms of viral membrane fusion and its inhibition, Annu. Rev. Biochem. 70 (2001) 777–810.
[3] J.M. White, S.E. Delos, M. Brecher, K. Schornberg, Structures and mechanisms of viral membrane fusion proteins: multiple variations on a common theme, Crit. Rev. Biochem. Mol. Biol. 43 (2008) 189–219.
[4] M. Kielian, F.A. Rey, Virus membrane-fusion proteins: more than one way to make a hairpin, Nat. Rev. Microbiol. 4 (2006) 67–76.
[5] R.M. Epand, Fusion peptides and the mechanism of viral fusion, Biochim. Biophys. Acta 1614 (2003) 116–121.
[6] Y.A. Klug, E. Rotem, R. Schwarzer, Y. Shai, Mapping out the intricate relationship of the HIV envelope protein and the membrane environment, Biochim. Biophys. Acta 1859 (2017) 550–560.
[7] L.K. Tamm, Hypothesis: spring-loaded boomerang mechanism of influenza hemagglutinin-mediated membrane fusion, Biochim. Biophys. Acta 1614 (2003) 14–23.
[8] B. Apellaniz, N. Huarte, E. Largo, J.L. Nieva, The three lives of viral fusion peptides, Chem. Phys. Lipids 181 (2014) 40–55.
[9] R. Blumenthal, S. Durell, M. Viard, HIV entry and envelope glycoprotein-mediated fusion, J. Biol. Chem. 287 (2012) 40841–40849.
[10] H. Badani, R.F. Garry, W.C. Wimley, Peptide entry inhibitors of enveloped viruses: the importance of interfacial hydrophobicity, Biochim. Biophys. Acta 1838 (2014) 2180–2197.
[11] T. Matthews, M. Salgo, M. Greenberg, J. Chung, R. DeMasi, D. Bolognesi, Enfuvirtide: the first therapy to inhibit the entry of HIV-1 into host CD4 lymphocytes, Nat. Rev. Drug Discov. 3 (2004) 215–225.
[12] C. Mathieu, M.T. Augusto, S. Niewiesk, B. Horvat, L.M. Palermo, G. Sanna, S. Madeddu, D. Huey, M.A. Castanho, M. Porotto, N.C. Santos, A. Moscona, Broad spectrum antiviral activity for paramyxoviruses is modulated by biophysical properties of fusion inhibitory peptides, Sci. Rep. 7 (2017) 43610, http://dx.doi.org/10.1038/srep43610.
[13] M.J. Gómara, V. Sánchez-Merino, A. Païs, A. Merino-Mansilla, J.M. Gatell, E. Yuste, I. Haro, Definition of an 18-mer synthetic peptide derived from the GB virus C E1 protein as a new HIV-1 entry inhibitor, Biochim. Biophys. Acta 1860 (2016) 1139–1148.
[14] Y.M. Hrobowski, R.F. Garry, S.F. Michael, Peptide inhibitors of dengue virus and West Nile virus infectivity, Virol. J. 2 (2005) 49.
[15] W. Weissenhorn, A. Hinz, Y. Gaudin, Virus membrane fusion, FEBS Lett. 581 (2007) 2150–2155.
[16] L.J. Earp, S.E. Delos, H.E. Park, J.M. White, The many mechanisms of viral membrane fusion proteins, Curr. Top. Microbiol. Immunol. 285 (2005) 25–66.
[17] A.E. Smith, A. Helenius, How viruses enter animal cells, Science 304 (2004) 237–242.
[18] S.C. Harrison, Viral membrane fusion, Nat. Struct. Mol. Biol. 15 (2008) 690–698.
[19] P. Guardado-Calvo, E.A. Bignon, E. Stettner, S.A. Jeffers, J. Pérez-Vargas, G. Pehau-Arnaudet, M.A. Tortorici, J.L. Jestin, P. England, N.D. Tischler, F.A. Rey, Mechanistic insight into bunyavirus-induced membrane fusion from structure-function analyses of the hantavirus envelope glycoprotein Gc, PLoS Pathog. 12 (2016) e1005813, , http://dx.doi.org/10.1371/journal.ppat.1005813.
[20] R. Worch, J. Krupa, A. Filipek, A. Szymaniec, P. Setny, Three conserved C-terminal residues of influenza fusion peptide alter its behavior at the membrane interface, Biochim. Biophys. Acta 1861 (2017) 97–105.
[21] Y.A. Klug, A. Ashkenazi, M. Viard, Z. Porat, R. Blumenthal, Y. Shai, Early and late HIV-1 membrane fusion events are impaired by sphinganine lipidated peptides that target the fusion site, Biochem. J. 461 (2014) 213–222.
[22] N.S. Alves, Y.S. Mendes, T.L. Souza, M.L. Bianconi, J.L. Silva, A.M. Gomes, A.C. Oliveira, A biophysical characterization of the interaction of a hepatitis C virus membranotropic peptide with micelles, Biochim. Biophys. Acta 1864 (2016) 359–371.
[23] P.U. Ratnayake, K. Sackett, M.J. Nethercott, D.P. Weliky, pH-dependent vesicle fusion induced by the ectodomain of the human immunodeficiency virus membrane fusion protein gp41: two kinetically distinct processes and fully-membrane-associated gp41 with predominant β sheet fusion peptide conformation, Biochim. Biophys. Acta 1848 (2015) 289–298.
[24] X. Han, J.H. Bushweller, D.S. Cafiso, L.K. Tamm, Membrane structure and fusion-triggering conformational change of the fusion domain from influenza hemagglutinin, Nat. Struct. Biol. 8 (2001) 715–720.
[25] J.L. Lorieau, J.M. Louis, A. Bax, The complete influenza hemagglutinin fusion domain adopts a tight helical hairpin arrangement at the lipid: water interface, Proc. Natl. Acad. Sci. U. S. A. 107 (2010) 11341–11346.
[27] A. Agopian, M. Quetin, S. Castano, A biophysical characterization of the interaction of a hepatitis C virus membranotropic peptide with micelles, Biochim. Biophys. Acta 1858 (2016) 2671–2680.
[28] S.M. Gregory, E. Harada, B. Liang, S.E. Delos, J.M. White, L.K. Tamm, Structure and function of the complete internal fusion loop from ebolavirus glycoprotein 2, Proc. Natl. Acad. Sci. U. S. A. 108 (2011) 11211–11216.
[29] G. Lu, Q. Wang, F.G. Gao, Bat-to-human: spike features determining 'host jump' of coronaviruses SARS-CoV, MERS-CoV, and beyond, Trends Microbiol. 8 (2015) 468–478.
[30] R.A. Weinstein, Planning for epidemics-the lessons of SARS, N. Engl. J. Med. 350 (2004) 2332–2334.
[31] K.V. Holmes, Structural biology. Adaptation of SARS coronavirus to humans, Science 309 (2005) 1822–1823.
[32] M. Bolles, E. Donaldson, R. Baric, SARS-CoV and emergent coronaviruses: viral determinants of interspecies transmission, Curr. Opin. Virol. 6 (2011) 624–634.
[33] A.M. Zaki, S. van Boheemen, T.M. Bestebroer, A.D. Osterhaus, R.A. Fouchier, Isolation of a novel coronavirus from a man with pneumonia in Saudi Arabia, N. Engl. J. Med. 367 (2012) 1814–1820.
[34] J.A. Al-Tawfiq, Z.A. Memish, Middle East respiratory syndrome coronavirus: transmission and phylogenetic evolution, Trends Microbiol. 22 (2014) 573–579.
[35] F.S. Aleanizy, N. Mohmed, F.Y. Alqahtani, El.H.R.A. Mohamed, Outbreak of Middle East respiratory syndrome coronavirus in Saudi Arabia: a retrospective study, BMC Infect. Dis. 17 (2017) 23.
[36] N.M. Okba, V.S. Raj, B.L. Haagmans, Middle East respiratory syndrome coronavirus vaccines: current status and novel approaches, Curr. Opin. Virol. 23 (2017) 49–58.
[37] E. de Wit, N. van Doremalen, D. Falzarano, V.J. Munster, SARS and MERS: recent insights into emerging coronaviruses, Nat. Rev. Microbiol. 8 (2016) 523–534.
[38] T.M. Gallagher, M.J. Buchmeier, Coronavirus spike proteins in viral entry and pathogenesis, Virology 279 (2001) 371–374.
[39] F. Li, W. Li, M. Farzan, S.C. Harrison, Structure of SARS coronavirus spike receptor-binding domain complexed with receptor, Science 309 (2005) 1864–1868.
[40] F. Taguchi, Y.K. Shimazaki, Functional analysis of an epitope in the S2 subunit of the murine coronavirus spike protein: involvement in fusion activity, J. Gen. Virol. 81 (2000) 2867–2871.
[41] B.J. Bosch, R. van der Zee, C.A. de Haan, P.J. Rottier, The coronavirus spike protein is a class I virus fusion protein: structural and functional characterization of the fusion core complex, J. Virol. 77 (2003) 8801–8811.
[42] B.J. Bosch, B.E. Martina, R. Van Der Zee, J. Lepault, B.J. Haijema, C. Versluis, A.J. Heck, R. De Groot, A.D. Osterhaus, P.J. Rottier, Severe acute respiratory syndrome coronavirus (SARS-CoV) infection inhibition using spike protein heptad repeat-derived peptides, Proc. Natl. Acad. Sci. U. S. A. 101 (2004) 8455–8460.
[43] M. Gui, W. Song, H. Zhou, J. Xu, S. Chen, Y. Xiang, X. Wang, Cryo-electron microscopy structures of the SARS-CoV spike glycoprotein reveal a prerequisite conformational state for receptor binding, Cell Res. 1 (2017) 119–129.
[44] Y. Xu, Z. Lou, Y. Liu, H. Pang, P. Tien, G.F. Gao, Z. Rao, Crystal structure of severe acute respiratory syndrome coronavirus spike protein fusion core, J. Biol. Chem. 279 (2004) 49414–49419.
[45] V.M. Supekar, C. Bruckmann, P. Ingallinella, E. Bianchi, A. Pessi, A. Carfi, Structure of a proteolytically resistant core from the severe acute respiratory syndrome coronavirus S2 fusion protein, Proc. Natl. Acad. Sci. U. S. A. 101 (2004) 17958–17963.
[46] Y. Deng, J. Liu, Q. Zheng, W. Yong, M. Lu, Structures and polymorphic interactions of two heptad-repeat regions of the SARS virus S2 protein, Structure 14 (2006) 889–899.
[47] S. Hakansson-McReynolds, S. Jiang, L. Rong, M. Caffrey, Solution structure of the severe acute respiratory syndrome-coronavirus heptad repeat 2 domain in the prefusion state, J. Biol. Chem. 281 (2006) 11965–11971.
[48] B. Sainz Jr., J.M. Rausch, W.R. Gallaher, R.F. Garry, W.C. Wimley, Identification and characterization of the putative fusion peptide of the severe acute respiratory syndrome-associated coronavirus spike protein, J. Virol. 79 (2005) 7195–7206.
[49] J. Guillen, A.J. Perez-Berna, M.R. Moreno, J. Villalain, Identification of the membrane-active regions of the severe acute respiratory syndrome coronavirus spike membrane glycoprotein using a 16/18-mer peptide scan: implications for the viral fusion mechanism, J. Virol. 79 (2005) 1743–1752.
[50] J. Guillen, A.J. Perez-Berna, M.R. Moreno, J. Villalain, A second SARS-CoV S2 glycoprotein internal membrane-active peptide. Biophysical characterization and membrane interaction, Biochemistry 47 (2008) 8214–8224.
[51] B. Sainz Jr., J.M. Rausch, W.R. Gallaher, R.F. Garry, W.C. Wimley, The aromatic domain of the coronavirus class I viral fusion protein induces membrane permeabilization: putative role during viral entry, Biochemistry 44 (2005) 947–958.

[52] X. Ou, W. Zheng, Y. Shan, Z. Mu, S.R. Dominguez, K.V. Holmes, Z. Qian, Identification of the fusion peptide-containing region in betacoronavirus spike glycoproteins, J. Virol. 90 (2016) 5586–5600.
[53] L.G. Basso, E.F. Vicente, E. Crusca, E.M. Cilli, A.J. Costa-Filho, SARS-CoV fusion peptides induce membrane surface ordering and curvature, Sci Rep 6 (2016) 37131, http://dx.doi.org/10.1038/srep37131.
[54] J. Guillen, P.K. Kinnunen, J. Villalain, Membrane insertion of the three main membranotropic sequences from SARS-CoV S2 glycoprotein, Biochim. Biophys. Acta 1778 (2008) 2765–2774.
[55] I.G. Madu, S.L. Roth, S. Belouzard, G.R. Whittaker, Characterization of a highly conserved domain within the severe acute respiratory syndrome coronavirus spike protein S2 domain with characteristics of a viral fusion peptide, J. Virol. 83 (2009) 7411–7421.
[56] M. Mahajan, S. Bhattacharjya, NMR structures and localization of the potential fusion peptides and the pre-transmembrane region of SARS-CoV: implications in membrane fusion, Biochim. Biophys. Acta 1848 (2015) 721–730.
[57] M. Mahajan, S. Bhattacharjya, Designed di-heme binding helical transmembrane protein, Chembiochem 15 (2014) 1257–1262.
[58] S. Bhattacharjya, P. Xu, H. Xiang, M. Chrétien, N.G. Seidah, F. Ni, pH-induced conformational transitions of a molten-globule-like state of the inhibitory prodomain of furin: implications for zymogen activation, Protein Sci. 5 (2001) 934–942.
[59] S. Bhattacharjya, P. Xu, P. Wang, M.J. Osborne, F. Ni, Conformational analyses of a partially-folded bioactive prodomain of human furin, Biopolymers 86 (2007) 329–344.
[60] A.S. Ingris, Cleavage at aspartic acid, Methods Enzymol. 91 (1983) 324–332.
[61] D.S. Wishart, C.G. Bigam, J. Yao, F. Abildgaard, H.J. Dyson, E. Oldfield, J.L. Markley, B.D. Sykes, ^{1}H, ^{13}C and ^{15}N chemical shift referencing in biomolecular NMR, J. Biomol. NMR 6 (1995) 135–140.
[62] D.K. Struck, D. Hoekstra, R.E. Pagano, Use of resonance energy transfer to monitor membrane fusion, Biochemistry 20 (1981) 4093–4099.
[63] H. Mohanram, A. Nip, P.N. Domadia, A. Bhunia, S. Bhattacharjya, NMR structure, localization, and vesicle fusion of chikungunya virus fusion peptide, Biochemistry 51 (2012) 7863–7872.
[64] H. Wang, P. Yang, K. Liu, F. Guo, Y. Zhang, G. Zhang, C. Jiang, SARS coronavirus entry into host cells through a novel clathrin- and caveolae-independent endocytic pathway, Cell Res. 18 (2008) 290–301.
[65] D.S. Wishart, Interpreting protein chemical shift data, Prog. Nucl. Magn. Reson. Spectrosc. 58 (2011) 62–87.
[66] L. Buchner, P. Güntert, Systematic evaluation of combined automated NOE assignment and structure calculation with CYANA, J. Biomol. NMR 62 (2015) 81–95.
[67] P. Damberg, J. Jarvet, A. Graslund, Micellar systems as solvents in peptide and protein structure determination, Methods Enzymol. 339 (2001) 271–285.
[68] C. Hilty, G. Wider, C. Fernandez, K. Wuthrich, Membrane protein-lipid interactions in mixed micelles studied by NMR spectroscopy with the use of paramagnetic reagents, Chembiochem 5 (2004) 467–473.
[69] O. Samuel, Y. Shai, Participation of two fusion peptides in measles virus-induced membrane fusion: emerging similarity with other paramyxoviruses, Biochemistry 40 (2001) 1340–1349.
[70] M.R. Moreno, R. Pascual, J. Villalain, Identification of membrane-active regions of the HIV-1 envelope glycoprotein gp41 using a 15-mer gp41-peptide scan, Biochim. Biophys. Acta 1661 (2004) 97–105.
[71] S.G. Peisajovich, Y. Shai, Viral fusion proteins: multiple regions contribute to membrane fusion, Biochim. Biophys. Acta 1614 (2003) 122–129.
[72] U. Ghosh, L. Xie, L. Jia, S. Liang, D.P. Weliky, Closed and semiclosed interhelical structures in membrane vs closed and open structures in detergent for the influenza virus hemagglutinin fusion peptide and correlation of hydrophobic surface area with fusion catalysis, J. Am. Chem. Soc. 137 (2015) 7548–7551.
[73] A.C. Walls, M.A. Tortorici, B.J. Bosch, B. Frenz, P.J. Rottier, F. DiMaio, F.A. Rey, D. Veesler, Cryo-electron microscopy structure of a coronavirus spike glycoprotein trimer, Nature 531 (2016) 114–117.
[74] R.N. Kirchdoerfer, et al., Pre-fusion structure of a human coronavirus spike protein, Nature 531 (2016) 118–121.
[75] K. Sackett, M.J. Nethercott, Z. Zheng, D.P. Weliky, Solid-state NMR spectroscopy of the HIV gp41 membrane fusion protein supports intermolecular antiparallel beta sheet fusion peptide structure in the final six-helix bundle state, J. Mol. Biol. 426 (2014) 1077–1094.
[76] B. Sainz Jr., E.C. Mossel, W.R. Gallaher, W.C. Wimley, C.J. Peters, R.B. Wilson, R.F. Garry, Inhibition of severe acute respiratory syndrome-associated coronavirus (SARS-CoV) infectivity by peptides analogous to the viral spike protein, Virus Res. 120 (2006) 146–155.
[77] L. Lu, et al., Structure-based discovery of Middle East respiratory syndrome coronavirus fusion inhibitor, Nat. Commun. 5 (2014) 3067, http://dx.doi.org/10.1038/ncomms4067.